Thermometry and Memcapacitance with a Qubit-Resonator System

S. N. Shevchenko[1,2,*] and D. S. Karpov[1,3]

[1] *B. I. Verkin Institute for Low Temperature Physics and Engineering, Kharkov, Ukraine*
[2] *V. N. Karazin Kharkov National University, Kharkov, Ukraine*
[3] *Leibniz Institute of Photonic Technology, Jena, Germany*

(Received 19 January 2018; revised manuscript received 10 May 2018; published 16 July 2018)

We study theoretically the dynamics of a driven-dissipative qubit-resonator system. Specifically, a transmon qubit is coupled to a transmission-line resonator; this system is considered to be probed via a resonator, by means of either continuous or pulsed measurements. Analytic results obtained in the semiclassical approximation are compared with calculations in the semiquantum theory as well as with the previous experiments. We demonstrate that the temperature dependence of the resonator frequency shift can be used for the system thermometry and that the dynamics, which display a pinched-hysteretic curve, can be useful for realization of the memory devices termed quantum memcapacitors.

DOI: 10.1103/PhysRevApplied.10.014013

I. INTRODUCTION

The key object in up-to-date circuit quantum electrodynamics (QED) is the system comprised of a qubit coupled to the quantum transmission-line resonator [1]. Such systems are useful both for studying fundamental quantum phenomena and for quantum information protocols, including control, readout, and memory [2,3]. A realistic QED system also includes electronics for driving and probing, while general considerations should, in addition, include the inevitable dissipative environment and nonzero temperature.

In many cases, the temperature can be assumed to be equal to zero. However, there are situations when it is important both to take into account and to monitor the effective temperature [4,5]. One of the reasons is that it is a variable value, which depends on several factors [6–8]; for example, it varies significantly with increasing driving power. Different aspects of thermometry involving qubits have been studied in Refs. [9–15].

Even though our considerations are quite general and can be applied to other types of qubit-resonator systems, including semiconductor qubits [16], for concreteness we concentrate on a transmon-type qubit in a cavity, a versatile study was presented in Ref. [17]. These systems have been studied from differing perspectives, recently including such an elaborate phenomenon as Landau-Zener-Stückelberg-Majorana interference [18]. The impact of the temperature was studied in Ref. [10]; however, the authors were mainly interested in the resonator temperature. Here, we explicitly take into account the nonzero effective temperature impact on both the resonator and the qubit. First, we obtain simplified but transparent analytic expressions for the transmission coefficient in the semiclassical approximation, which ignores the qubit-resonator correlations. Such a semiclassical approach is useful, but its validity should be checked [19]. For this reason, we further develop our calculations by taking into account the qubit-resonator correlators.

Having obtained agreement with previous experiments, such as those described in Refs. [17,20,21], we also consider another emergent application for memory devices. Different types of memory devices, such as memcapacitors and meminductors, have been introduced in addition to memristors [22,23]. For different proposals concerning superconducting memory elements, see also Refs. [24–26]. Quantum versions of memristors, memcapacitors, and meminductors have been discussed in Refs. [27–31]. In particular, in Ref. [28] it has been suggested that a charge qubit can behave as a quantum memcapacitor. Here, we consider a transmon qubit in a cavity, instead of a charge qubit, as a possible candidate for the realization of the quantum memcapacitor. For this, we demonstrate that the transmon-resonator system can be described by the relations that define a memcapacitor.

Overall, the paper is organized as follows. In Sec. II, we consider the driven qubit-resonator system probed via quadratures of the transmitted field. This is developed by taking temperature into account in Sec. III, where continuous measurements are considered. While we compare our results with those of Ref. [17], our approach there (also presented in Appendix A), was the semiclassical theory, which is valid for both dispersive and resonant cases. Importantly, we verify the results with more

---

[*] sshevchenko@ilt.kharkov.ua

elaborate calculations, taking into account two-operator qubit-resonator correlators, the details of which are presented in Appendix B. Section IV is devoted to the case of single-shot pulsed measurements. In Sec. V, we consider cyclic dynamics with hysteretic dependencies, which are needed for emergent memory applications.

II. TIME DEPENDENCE OF THE QUADRATURES

The qubit-resonator system we consider is the circuit-QED realization, as studied in Refs. [1,17]. The qubit is the transmon formed by an effective Josephson junction and the shunt capacitance C_B; it is capacitively coupled to the transmission-line resonator via C_g, as shown in the inset of Fig. 1. The resonator is driven via C_{in} and the measured value is the transmitted electromagnetic field after C_{out}. In addition, the effective Josephson junction describes a loop with two junctions controlled by an external magnetic flux Φ; the respective Josephson capacitance and energy are denoted in the scheme by C_J and E_J respectively. The characteristic charging energy of a qubit is $E_c = e^2/2C_\Sigma$ with $C_\Sigma = C_J + C_B + C_g$.

The driven transmon-resonator system [1,17,32] is described by the Jaynes-Cummings Hamiltonian [33]

$$H = \hbar\omega_r a^\dagger a + \hbar\frac{\omega_q}{2}\sigma_z + \hbar g(\sigma a^\dagger + \sigma^\dagger a) + \hbar\xi\left(a^\dagger e^{-i\omega t} + a e^{i\omega t}\right). \tag{1}$$

Here, the transmon is considered in the two-level approximation, described by the energy distance $\hbar\omega_q$ between the levels and the Pauli operators σ_i and $\sigma_\pm = (\sigma_x \pm i\sigma_y)/2$, where we opt to use the ladder-operator notations $\sigma \equiv \sigma_-$ and $\sigma^\dagger \equiv \sigma_+$. The resonator is described by the resonant frequency ω_r and the annihilation operator a. The transmon-resonator coupling constant g relates to the bare coupling g_0 as $g = g_0\sqrt{E_c/|\Delta - E_c|}$ with $\Delta = \hbar(\omega_q - \omega_r)$ (this renormalization is due to the virtual transitions through the upper transmon's states). The probing signal is described by the amplitude ξ and frequency ω.

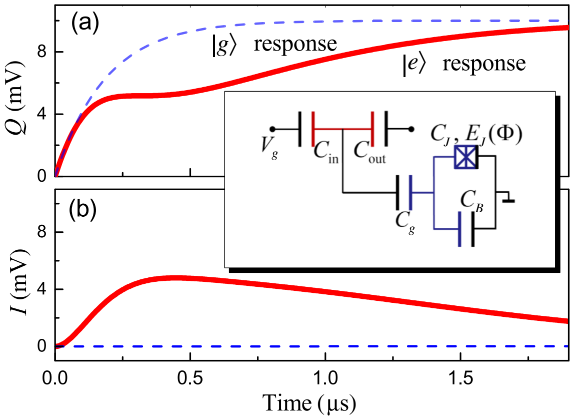

FIG. 1. Time evolution of the quadratures, (a) Q and (b) I , for the parameters of Ref. [17] for two situations, when the qubit was initialized in either the ground or excited state, denoted as "$|g\rangle$ response" and "$|e\rangle$ response," respectively. The inset presents the scheme of the transmon-type qubit coupled to the transmission-line resonator.

The system's dynamics obey the master equation, which is described in Appendix A. There, it is demonstrated that the Lindblad equation for the density matrix can be rewritten as an infinite set of equations for the expectation values. In Refs. [17,34], the set of equations was reduced to six complex equations for the single expectation values and the two-operator correlators. Meanwhile, many quantum-optical phenomena can be described within the semiclassical theory, assuming that all the correlation functions factorize (e.g., Refs. [35–38]). This approach results in the system's dynamics being described by a set of three equations only, Eqs. (A9), which are more suitable for analytic consideration, as we shall see below. This was also analyzed in Ref. [34]; in particular, the robustness of the semiclassical approximation was demonstrated even in the small-photon-number limit, at the small probing amplitude ξ.

The observable value can be either the transmission-signal amplitude or the quadrature amplitudes. The quadratures of the transmitted field I and Q are related to the cavity field $\langle a\rangle$ as follows [17,32]:

$$I = 2V_0\,\text{Re}\langle a\rangle, \quad Q = 2V_0\,\text{Im}\langle a\rangle, \tag{2}$$

where V_0 is a voltage related to the gain of the experimental amplification chain [32], defined as [17] $V_0^2 = Z\hbar\omega_r\kappa/4$, with Z denoting the transmission-line impedance. The transmission amplitude A is given [32,38] by the absolute value of $\langle a\rangle$:

$$A = \sqrt{I^2 + Q^2} = 2V_0|\langle a\rangle|. \tag{3}$$

As an illustration of the semiclassical theory, presented in more detail in Appendix A, consider the experimental realization in Ref. [17]. There, the qubit was initialized in either ground or excited state and then, by means of either continuous or pulsed measurements, the quadratures of the transmitted field were probed. Correspondingly, we make use of Eqs. (2) and (A9), which include the resonator relaxation rate κ and the qubit decoherence rate $\Gamma_2 = \Gamma_\phi + \Gamma_1/2$, where Γ_ϕ and Γ_1 are the intrinsic qubit pure dephasing and relaxation rates. We take the following parameters [17]: $\omega_r/2\pi = 6.4425$ GHz, $\omega_q/2\pi = 4.01$ GHz, $g_0/2\pi = 134$ MHz, $\kappa/2\pi = 1.7$ MHz, $\Gamma_1/2\pi = 0.2$ MHz, $\Gamma_2 = \Gamma_1/2$, $E_c/h = 232$ MHz, and $V_0 = 5$ mV, where the latter has been chosen as a fitting parameter. The results for low temperature (i.e., for $k_B T \ll \hbar\omega_q$) are presented in Fig. 1. Note the agreement with the experimental observations in Ref. [17]; see also the detailed calculations in Appendix B. In Ref. [17], it is discussed in detail that the relaxation of the quadratures is determined for the ground-state formulation by the resonator rate κ only, while for the excited-state formulation it is determined by the collaborative evolution of the qubit-resonator system. For example, one can observe that the relaxation of the quadratures in Fig. 1 for the "$|e\rangle$ response" happens in two stages, during the times $T_\kappa = 2\pi/\kappa \simeq 0.6\ \mu$s and $T_1 = 2\pi/\Gamma_1 \gg T_\kappa$.

III. THERMOMETRY WITH CONTINUOUS MEASUREMENTS

In the preceding section, we calculated the low-temperature behavior of the observable quadratures for the qubit-resonator system and illustrated this in Fig. 1. Having obtained agreement with the experimental observations of Ref. [17], we can proceed with posing other questions about the system. Consider now the sensitivity of the system to the changes of temperature. How does the behavior of the observables change? Is this useful for a single-qubit thermometry? To respond to such questions, we describe below both the dynamical and the stationary behavior for nonzero temperature.

In Fig. 2, we plot the time evolution of the quadratures for the same parameters as in Fig. 1 except for the temperature, which now is considered to be nonzero. Figure 2 demonstrates that both the evolutionary and stationary values (at long times, independent of the initial conditions) are strongly temperature dependent.

To further explore the temperature dependence, we now consider the steady-state measurements. In equilibrium, the observables are described by the steady-state values of $\langle a\rangle$, $\langle\sigma\rangle$, and $\langle\sigma_z\rangle$. The steady-state solution for the weak driving amplitude in the semiclassical approximation is as follows (for details, see Appendix A):

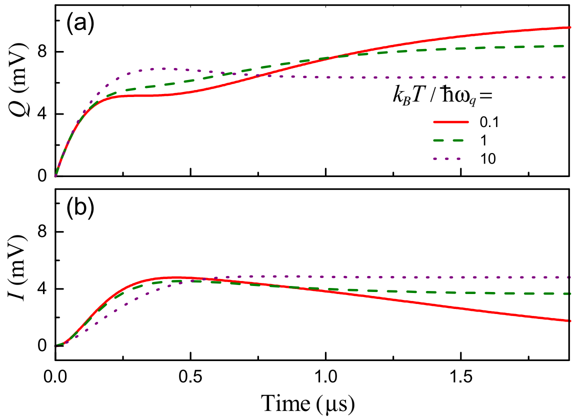

FIG. 2. Time evolution of the quadratures, (a) Q and (b) I, for nonzero temperature T. The situation when the qubit was initialized in the excited state is considered. The parameters are the same as in Fig. 1, besides the temperature, so that the solid red curves for low temperature repeat those from the preceding figure.

$$\langle a\rangle = -\xi\,\frac{\delta\omega_q'}{\langle\sigma_z\rangle g^2 + \delta\omega_q'\delta\omega_r'}, \tag{4}$$

where

$$\delta\omega_r' = \omega_r - \omega - i\frac{\kappa}{2}, \quad \delta\omega_q' = \omega_q - \omega - i\frac{\Gamma_2}{z_0}, \\ z_0 = \tanh\left(\frac{\hbar\omega_q}{2k_BT}\right). \tag{5}$$

In equilibrium, the qubit energy-level populations are defined by the temperature T: $\langle\sigma_z\rangle = -z_0$ [20]. Importantly, Eq. (4) bears information about the qubit temperature and, via Eq. (3), conveys this dependence to the observables.

Equation (4) is quite general. To start with, for an isolated resonator (without a qubit) at $g = 0$, this gives

$$|\langle a\rangle|^2 = \xi^2\frac{1}{\delta\omega_r^2 + \kappa^2/4}, \tag{6}$$

which defines the resonator width.

Consider now the *dispersive* limit, where $\Delta/\hbar \equiv \omega_q(\Phi) - \omega_r \gg g/h,\ \delta\omega_r$. Then we have for the transmission amplitude

$$|\langle a\rangle|^2 \approx \xi^2\frac{\Delta^2}{(\langle\sigma_z\rangle g^2 + \Delta\delta\omega_r)^2 + \Delta^2\kappa^2/4}. \tag{7}$$

This, in particular, gives the maxima for the transmission at

$$\delta\omega_r = -\langle\sigma_z\rangle\frac{g^2}{\Delta} \equiv -\langle\sigma_z\rangle\chi. \tag{8}$$

Then, for the ground or excited states with $\langle\sigma_z\rangle = \mp 1$, one obtains the two dispersive shifts for the maximal transmission, $\delta\omega_r = \pm\chi = \pm g_0^2E_c/\Delta(\Delta - E_c)$, respectively. In thermal equilibrium, Eq. (9) for the resonance frequency shift gives $\delta\omega_r(T) = (g^2/\Delta)\tanh(\hbar\omega_q/2k_BT)$.

Making use of Eqs. (3) and (7) in thermal equilibrium, when $\langle\sigma_z\rangle = -z_0$, in the inset of Fig. 3 we plot the frequency dependence of the transmission amplitude for the parameters of Ref. [17]. We plot two curves: the continuous one corresponds to a low-temperature limit ($z_0 = 1$), with the system in the ground state, and the dashed line is plotted in a high-temperature limit ($z_0 = 0$), with the system is in a superposition of the ground and excited states. The maximal frequency shift is denoted by χ. Note that the low-temperature limit (continuous line in the inset), with $\langle\sigma_z\rangle \sim -1$, corresponds to the ground state, while the high-temperature limit (dashed line), with $\langle\sigma_z\rangle \sim 0$, is equivalent to the absence of the qubit, at $g = 0$.

For varying temperature, the frequency shift is plotted in the main panel of Fig. 3 for the parameters of Ref. [17]. We note that a similar dependence can be found in Fig. 4.2 of Ref. [39]; the difference is in that in the case of Refs. [17,39], the similar change of $\langle\sigma_z\rangle$ from -1 to 0 was due to variation of the driving power. When driven at low power, the qubit stayed in the ground state with $\langle\sigma_z\rangle = -1$, while with increasing power its stationary state tended toward equally populated states with $\langle\sigma_z\rangle = 0$. We also devote Appendix C to this case of varying the driving of the qubit.

The temperature dependence in Fig. 3 becomes apparent at $T \geq T^*$, where $T^* = 0.1\hbar\omega_q/k_B$ is the characteristic temperature, which for, say, $\omega_q/2\pi = 4$ GHz is quite low, at $T^* = 20$ mK. This means that such measurements may be useful for realizing the *one-qubit thermometry* for $T \geq T^*$.

It is important to note that Eq. (4) was obtained without making use of the dispersive limit and thus is applicable to the opposite limit. Consider in this way $\omega_q(\Phi) = \omega_r$, which is the *resonant* limit, $\Delta = 0$. With equal detunings for both the qubit and the resonator, $\omega_q - \omega = \omega_r - \omega \equiv \delta\omega$, we can use the formula for the photon operator, Eq. (4), which gives

$$|\langle a\rangle|^2 \approx \xi^2 \frac{\delta\omega^2 + \Gamma_2^2/z_0^2}{(\langle\sigma_z\rangle g^2 + \delta\omega^2)^2 + \delta\omega^2(\Gamma_2/z_0 + \kappa/2)^2}. \quad (9)$$

With this result we plot the transmission amplitude as a function of the frequency detuning in Fig. 4 for different temperatures. Equation (9) describes maxima, which, assuming large cooperativity $g^2/\Gamma_2\kappa \gg 1$, are situated at $\delta\omega = 0$ (the high-temperature peak) and at

$$\delta\omega \approx \pm g \tanh^{1/2}\left(\frac{\hbar\omega_q}{2k_BT}\right). \quad (10)$$

The latter formula, in particular, in the low-temperature limit describes the peaks at $\delta\omega = \pm g$, which is known as the vacuum Rabi splitting. Note that recently such vacuum Rabi splitting has also been demonstrated in silicon qubits in Ref. [16]. With increasing qubit temperature, Eq. (10) describes the temperature-dependent resonance-frequency shift. We note that this shift is again described by the factor $\langle\sigma_z\rangle = -z_0$. If we assume here that the qubit is in the ground state, $\langle\sigma_z\rangle = -1$, then the increase of the temperature would result in suppressing the peaks at $\delta\omega = \pm g$ without their shifting, in agreement with Ref. [10].

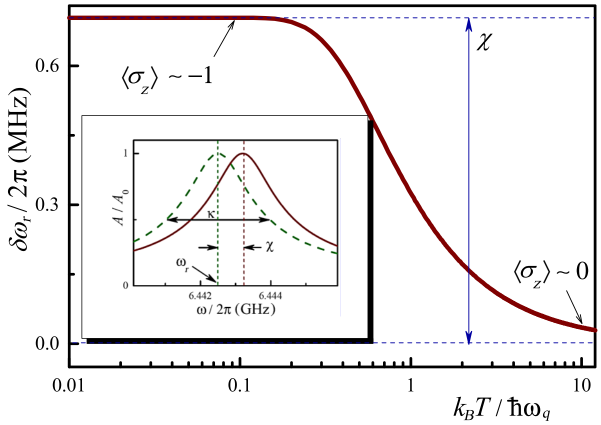

FIG. 3. Transmission amplitude and the frequency shift. First, the inset shows the transmission amplitude A versus the frequency ω when the qubit is either in the ground state (solid line) or in the excited state (dashed line). Then, the main panel demonstrates the frequency shift $\delta\omega_r = \omega_r - \omega$, corresponding to the frequency ω at which the transmission is maximal, plotted as a function of the temperature T. Here, the transmission amplitude is normalized with $A_0 = 4V_0g\xi/\kappa$.

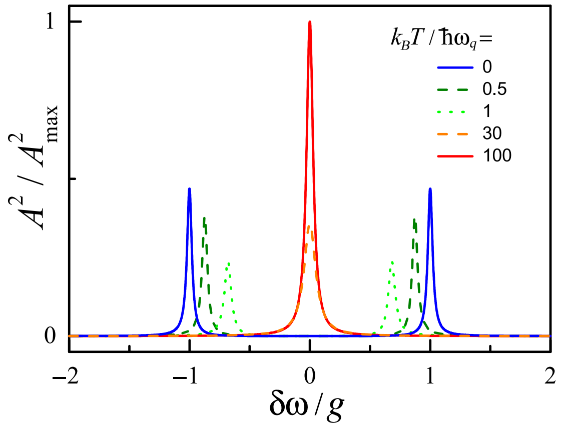

FIG. 4. Transmission, A^2, normalized to its maximal value $A_{\max}$, versus the frequency shift $\delta\omega$ for different values of temperature T.

IV. THERMOMETRY WITH PULSED MEASUREMENTS

Previously, we have considered the case when the measurement is done in a weak continuous manner. Then, the resonator probes the averaged qubit state, defined by $\langle\sigma_z\rangle$, and a change in the qubit state results in a shift in the position of the resonant transmission. Alternatively, measurements can be done with a single-shot readout [20,40–43]. In this case, in each measurement the resonator would "see" the qubit in either the ground or the excited state, with $\langle\sigma_z\rangle$ equal to -1 or 1, respectively [44]. The probability of finding the qubit in the excited state is P_+ and in the ground state is $P_- = 1 - P_+$. Then, the weighted (averaged over many measurements) transmission amplitude can be calculated as follows:

$$A = P_-A_- + P_+A_+, \quad (11)$$

where $A_\pm$ describe the transmission amplitudes calculated for $\langle\sigma_z\rangle = \pm 1$, respectively, as given by Eq. (7).

We may now consider two cases, first, of a qubit driven resonantly and, second, when the excitation happens due to the temperature. In the former case, when a qubit is driven with frequency $\omega_d = \omega_q$ and amplitude $\hbar\Omega$, the excited qubit state is populated with the probability

$$\begin{aligned} P_+(\Omega) &= \frac{1}{2}[1 + \overline{\Omega}^{-2}]^{-1}, \\ \overline{\Omega} &= \frac{1}{2}\hbar\Omega\sqrt{T_1 T_2}. \end{aligned} \tag{12}$$

This is obtained from the full formula for a qubit excited near the resonant frequency [34]:

$$P_+ = \frac{1}{2}\frac{\omega_q^2 J_1^2(\Omega/\omega_d)}{\omega_q^2 J_1^2(\Omega/\omega_d) + (T_2/T_1)(\omega_q - \omega_d)^2 + 1/T_1 T_2}, \tag{13}$$

where we then take $\omega_d = \omega_q$ and $J_1(x) \approx x/2$.

In thermal equilibrium, the upper-level occupation probability is defined by the Maxwell-Boltzmann distribution, $\langle\sigma_z\rangle = -z_0$ [20], so that $P_+ = \frac{1}{2}[1 + \langle\sigma_z\rangle]$ or

$$P_+(T) = \frac{1}{2}\left[1 - \tanh\left(\frac{\hbar\omega_q}{2k_B T}\right)\right]. \tag{14}$$

With Eqs. (12) and (14), we calculate the transmission amplitude, when the qubit is either resonantly driven (Fig. 5) or is in thermal equilibrium (Fig. 6), respectively. For the former case, we plot the frequency dependence of the transmission amplitude in Fig. 5. There would be a similar dependence for varying temperature; in Fig. 6, we present the transmission amplitude versus temperature for a fixed frequency $\omega = \omega_r + \chi = \omega_r - |\chi|$, where the excited-state peak appears. For our calculations here, we adopt parameters close to those of Ref. [20]: $\omega_r/2\pi = 10.976$ GHz, $\omega_q/2\pi = 4.97$ GHz, $\chi/2\pi = -4$ MHz, and we have chosen $\kappa/2\pi = 1$ MHz. Again, as above, we observe a strong dependence on temperature. The advantages of probing the qubit state in a similar manner were discussed in Ref. [40]. There, a proposal was put forward to probe a *driven* qubit state, while our proposal here relates to the *thermal*-equilibrium measurement and consists of providing a sensitive tool for thermometry. Indeed, a similar temperature dependence was recently observed by Jin *et al.* in Ref. [20]. In that work, the authors studied the excited-state occupation probability in a transmon with variable temperature. For comparison with that publication, in the inset of Fig. 6 we also present the low-temperature region, with a linear scale.

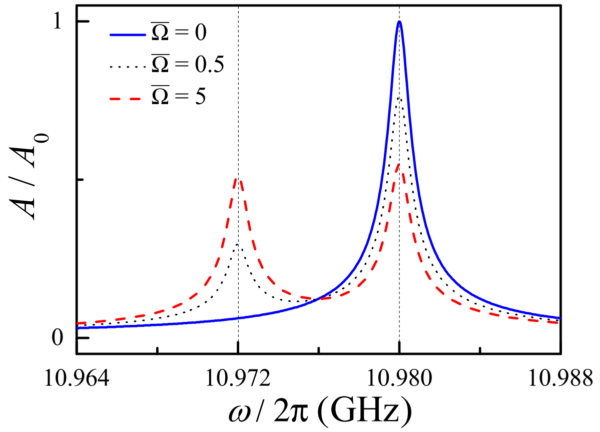

FIG. 5. Transmission amplitude for monitoring the state of a driven qubit. The frequency ω is in the range from $\omega_r - 3|\chi|$ to $\omega_r + 3|\chi|$. The peak corresponding to the ground state is at $\omega_r + |\chi| = 10.98$ GHz$\cdot 2\pi$. The peak appearing for nonzero occupation of the excited state is at $\omega = \omega_r - |\chi| = 10.972$ GHz$\cdot 2\pi$. The height of the latter is defined by the normalized driving amplitude $\overline{\Omega}$.

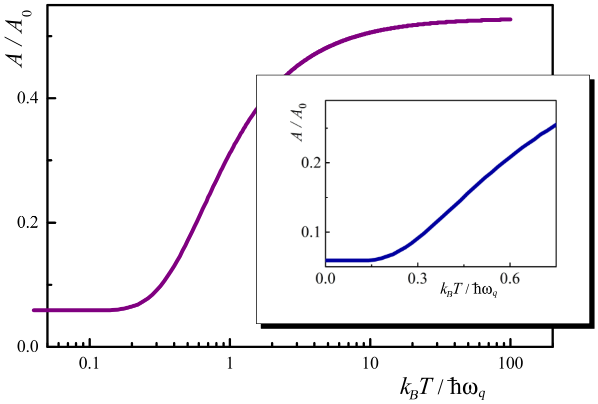

FIG. 6. Temperature dependence of the transmission amplitude A at the frequency corresponding to the excited-state peak, which is $\omega = \omega_r - |\chi|$ in the preceding figure. The inset shows the low-temperature region.

V. MEMCAPACITANCE

Now, having reached agreement between theory and experiment, we wish to explore other applications. In this section, we focus on possibilities for memory devices, such as memcapacitors.

In general, a memory device with input $u(t)$ and output $y(t)$ is, by definition, described by the following relations [22]:

$$y(t) = g(\mathbf{x}, u, t)u(t), \tag{15}$$

$$\dot{\mathbf{x}} = \mathbf{f}(\mathbf{x}, u, t). \tag{16}$$

Here, g is the response function, while the vector function $\mathbf{f}$ defines the evolution of the internal variables, denoted as a vector $\mathbf{x}$. Depending on the choice of the circuit variables u and y, the relations (15) and (16) describe memristive, meminductive, or memcapacitive systems. The particular case of voltage-controlled memcapacitive systems, defined

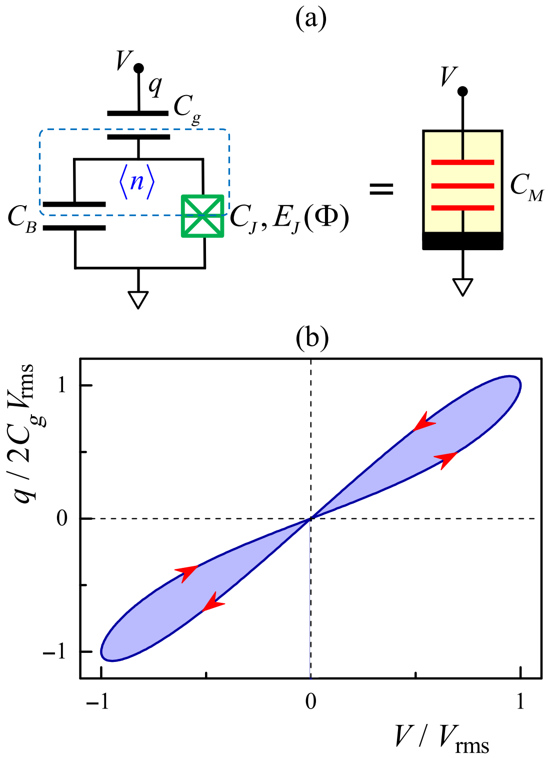

FIG. 7. A transmon qubit can be considered as a memcapacitor. (a) Scheme for a transmon-type qubit is shown to be equivalent to a memcapacitor C_M, the symbol for which is shown to the right. (b) Pinched-hysteretic curve in the voltage-charge plane as a fingerprint of memcapacitive behavior.

by the relations

$$q(t) = C_M(\mathbf{x}, V, t)V(t), \tag{17}$$

$$\dot{\mathbf{x}} = \mathbf{f}(\mathbf{x}, V, t), \tag{18}$$

is relevant for our considerations. Here, the response function C_M is called the memcapacitance.

Relations (15) and (16) and their particular cases, Eqs. (17) and (18), were related to diverse systems, as described, e.g., in the review article [23]. It was shown that the reinterpretation of known phenomena in terms of these relations makes them useful for memory devices. However, until recently their quantum analogs remained unexplored. Then, some similarities with and distinctions from classical systems were analyzed in Refs. [27–31]. In particular, it was argued that in the case of quantum systems, the circuit input and output variables u and y should be interpreted as quantum-mechanically-averaged values or given an ensemble interpretation [28,29]. Detailed analysis of diverse systems [27–31] has demonstrated that, as described by relations (15) and (16), quantum systems could be considered as quantum memristors, meminductors, and memcapacitors. These indeed display pinched-hysteresis loops for a periodic input, while the frequency dependence may differ significantly from that of the related classical devices. The former distinction is due to the probabilistic character of measurements in quantum mechanics. Note that the “pinched-hysteretic loop” dependence is arguably the most important property of memristors, meminductors, and memcapacitors [22,23].

It is thus our goal in this section to demonstrate how the evolution equations for a qubit-resonator system can be written in the form of the memcapacitor relations, Eqs. (17) and (18). This would allow us to identify the related input and output variables, the internal-state variables, and the response and evolution functions. As further evidence, we shall demonstrate one particular example, when for resonant driving, a pinched-hysteresis loop appears.

The transmon treated as a memcapacitor is depicted in Fig. 7(a). As an input of such a memcapacitor, we assume the resonator antinode voltage V (how a transmon is coupled to a transmission-line resonator is shown in Fig. 1), while the output is the charge q on the external plate of the gate capacitor C_g. One should differentiate between the externally applied voltage, $V_g = V_A \sin\omega t$, and the quantized antinode voltage,

$$V = \langle\widehat{V}\rangle = V_{\rm rms}\langle a e^{-i\omega t} + a^{\dagger} e^{i\omega t}\rangle = 2V_{\rm rms}\,\mathrm{Re}\langle a e^{-i\omega t}\rangle, \tag{19}$$

where $V_{\rm rms} = \sqrt{\hbar\omega_r/2C_r}$ is the root-mean-square voltage of the resonator, defined by its resonant frequency ω_r and capacitance C_r [1]. This observation makes the difference compared to a charge qubit coupled directly to a gate, such as in Ref. [28]. According to Eq. (19), the voltage is related to the measurable values, the resonator output field quadratures, given in Eq. (2). The charge q is related to the voltage V and the island charge $2e\langle n\rangle$ ($\langle n\rangle$ is the average Cooper-pair number) as follows [28]:

$$q = C_{\rm geom}V + \frac{C_g}{C_\Sigma}2e\langle n\rangle \equiv C_M V, \tag{20}$$

where we have formally introduced the memcapacitance C_M as a proportionality coefficient between the input V and the output q. Given the leading role of the shunt capacitance, here we have $C_\Sigma = C_J + C_g + C_B \sim C_B$ and $C_{\rm geom} = C_g(C_J + C_B)/C_\Sigma \approx C_g$. The number operator n is defined by the qubit Pauli matrix σ_y: $n = \frac{1}{4}\sqrt{\hbar\omega_q/E_c}\sigma_y$. This allows us to rewrite Eq. (20) as follows:

$$\widetilde{q} = \mathrm{Re}\langle a\rangle\cos\omega t - \mathrm{Im}\langle a\rangle\sin\omega t + \lambda\langle\sigma_y\rangle, \tag{21}$$

where $\widetilde{q} = q/2C_g V_{\rm rms}$ and $\lambda = (e/4C_\Sigma V_{\rm rms})\sqrt{\hbar\omega_q/E_c}$. We note that in related experiments, not only the quadratures I and Q (which define $\mathrm{Re}\langle a\rangle$ and $\mathrm{Im}\langle a\rangle$), but also the qubit state, defined by the values $\langle\sigma_z\rangle$ and $\langle\sigma_y\rangle$, can be reliably probed (see Refs. [17,18,45–47]). Importantly, the memcapacitor’s dynamics, i.e. $q(t)$, are defined by the rich dynamics of both the resonator and the qubit, via $\langle a\rangle$ and $\langle\sigma_y\rangle$, respectively.

Importantly, here we have written the transmon-resonator equations in the form of the first memcapacitor relation, Eq. (17). We can see that the role of the internal variables is played by the qubit charge $\langle n\rangle$. In its turn, the qubit state is defined by the Lindblad equation, which now takes the place of the second memcapacitor relation, Eq. (18). Such a formulation demonstrates that our qubit-resonator system can be interpreted as a quantum memcapacitor, which is schematically displayed in Fig. 7(a).

The above formulas allow us to plot the charge-versus-voltage diagram. We now assume that the qubit is driven by a field with amplitude Ω and frequency ω_d, which is resonant: $\omega_d = \omega_q(\Phi)$. This induces Rabi oscillations in the qubit with frequency Ω. By numerically solving Eqs. (5a)–(5d) in Ref. [17], we plot the q versus V diagram in Fig. 7(b). To obtain the pinched-hysteresis-type loop, we take the driving amplitude, $\Omega = 2\omega_r$, which corresponds to the strong-driving regime. The other system parameters are the same as used above (those of Ref. [17]) and $\lambda = 0.2$. In addition, we have taken $\mathrm{Re}\langle a\rangle = 0$ and $\mathrm{Im}\langle a\rangle = 1$. Here, we note that $\langle a\rangle$ is a slow function of time, as demonstrated in Fig. 1. (The characteristic time for this is $2\pi/\kappa$, which is $\gg 2\pi/\Omega$.) Moreover, the diagram is not only defined by λ (which is a constant), but also by $\langle a\rangle$ (which can be adjusted, for example, by choosing a moment of time in Fig. 1); so, for a different value of λ, another value of $\langle a\rangle$ can be taken. We note that the shaded area in Fig. 7(b) is equivalent to the energy consumed by the memcapacitor $\int VIdt$ [23].

Note that we use the two-level approximation for the transmon and also the strong-driving regime, where $\Omega = 2\omega_r$, which is needed in order to demonstrate the pinched-hysteresis loop by illustrative means. While the strong-driving regime has been demonstrated in many types of qubits, it is complicated for the transmon qubits due to the weak anharmonicity, which may result in transitions to the upper levels (cf., however, Refs. [18,48,49]). In this way, one would have to confirm the calculations with more elaborate ones, by taking the higher levels into account (as, e.g., in Refs. [21,50,51]; and see also our discussion in Appendix C) and to clarify the relation needed for the hysteretic-type loops. Alternatively, one may consider the readily observed Rabi oscillations in the megahertz domain and combine these with the oscillations related to another resonator. At such a low frequency, the resonator may be considered as classical, similar to the calculations in Ref. [28].

VI. CONCLUSION

We have considered the qubit-resonator system, focusing on the situation with a transmon-type qubit in a transmission-line resonator. The most straightforward approach is the semiclassical theory, in which all the correlators are assumed to factorize, which has the advantage of getting transparent analytic equations and formulas. We have demonstrated that with this system, we can describe relevant experiments [17,20,21]. On the other hand, the validity of the semiclassical theory has been checked by means of the approach taking into account the two-operator qubit-photon correlators, the so-called semiquantum approach. Furthermore, we have taken the temperature into consideration and studied its impact on the measurable quadratures of the transmitted field. Because of the qubit-resonator entanglement, the resonator transmission bears information about the temperature experienced by the qubit. Consideration of this application, the thermometry, was followed by another consideration, the memory device known as a memcapacitor. As a proof of concept, we have plotted the pinched-hysteretic loop in the charge-voltage plane, the fingerprint of memcapacitance. In the case with qubits, this loop is related to Rabi-type oscillations. We believe that such quantum memcapacitors, along with quantum meminductors and memristors, will add new functionality to the toolbox of their classical counterparts.

ACKNOWLEDGMENTS

We are grateful to A. Fedorov for stimulating discussions and critical comments, to S. Ashhab for critically reading the manuscript and for comments, and to Y. V. Pershin and E. Il'ichev for fruitful discussions. S.N.S. acknowledges the hospitality of the School of Mathematics and Physics of the University of Queensland, where part of this work was done. This work was partly supported by the State Fund for Fundamental Research of Ukraine (project Grants No. F66/95-2016) and DAAD Binationally Supervised Doctoral Degrees, 2017/18 (Grant No. 57299293).

APPENDIX A: LINDBLAD AND MAXWELL-BLOCH EQUATIONS

We consider how, starting from Hamiltonian (1), we get the motion equations in the semiclassical approximation and obtain the steady-state value for the photon operator in Eq. (4). First, Hamiltonian (1) is transformed using the operator $U = \exp[i\omega t(a^\dagger a + \sigma_z/2)]$ to the following $H' = UHU^\dagger + i\hbar\dot{U}U^\dagger$ (see, e.g., Ref. [34]):

$$H' = \hbar\delta\omega_r a^\dagger a + \hbar\frac{\delta\omega_q}{2}\sigma_z + \hbar g(\sigma a^\dagger + \sigma^\dagger a) + \hbar\xi(a^\dagger + a), \tag{A1}$$

where

$$\delta\omega_r = \omega_r - \omega, \quad \delta\omega_q = \omega_q - \omega. \tag{A2}$$

Then, the system's dynamics are described by the Lindblad master equation

$$\dot{\rho} = -\frac{i}{\hbar}[H', \rho] + \kappa\mathcal{D}[a]\rho + \Gamma_1\mathcal{D}[\sigma]\rho + \frac{\Gamma_\phi}{2}\mathcal{D}[\sigma_z]\rho, \tag{A3}$$

where the damping terms model the loss of cavity photons at rate κ, as well as the intrinsic qubit relaxation and pure dephasing at rates Γ_1 and Γ_ϕ. The respective Lindblad damping superoperators at nonzero temperature T are given by [52]

$$\mathcal{D}[a]\rho = (N_{\rm th} + 1)\left(a\rho a^\dagger - \frac{1}{2}\{a^\dagger a, \rho\}\right) + N_{\rm th}\left(a^\dagger\rho a - \frac{1}{2}\{aa^\dagger, \rho\}\right), \tag{A4a}$$

$$\mathcal{D}[\sigma]\rho = (n_{\rm th} + 1)\left(\sigma\rho\sigma^\dagger - \frac{1}{2}\{\sigma^\dagger\sigma, \rho\}\right) + n_{\rm th}\left(\sigma^\dagger\rho\sigma - \frac{1}{2}\left\{\sigma\sigma^\dagger, \rho\right\}\right), \tag{A4b}$$

$$\mathcal{D}[\sigma_z]\rho = (2n_{\rm th} + 1)(\sigma_z\rho\sigma_z - \rho), \tag{A4c}$$

$$N_{\rm th} = \left[\exp\left(\frac{\hbar\omega_r}{k_BT}\right) - 1\right]^{-1}, \quad n_{\rm th} = \left[\exp\left(\frac{\hbar\omega_q}{k_BT}\right) - 1\right]^{-1}. \tag{A5}$$

In particular, at $T = 0$, $N_{\rm th} = n_{\rm th} = 0$.

From the Lindblad equation, Eq. (A3), for the expectation values of the operators a, σ, and σ_z we obtain the following system of equations (as in Refs. [34,36]):

$$\frac{d\langle a\rangle}{dt} = -i\delta\omega_r'\langle a\rangle - ig\langle\sigma\rangle - i\xi, \tag{A6a}$$

$$\frac{d\langle\sigma\rangle}{dt} = -i\delta\omega_q'\langle\sigma\rangle + ig\langle a\sigma_z\rangle, \tag{A6b}$$

$$\frac{d\langle\sigma_z\rangle}{dt} = -i2g(\langle a\sigma^\dagger\rangle - \langle a^\dagger\sigma\rangle) - \Gamma_1\left(1 + \frac{\langle\sigma_z\rangle}{z_0}\right), \tag{A6c}$$

where

$$\delta\omega_r' = \delta\omega_r - i\frac{\kappa}{2}, \quad \delta\omega_q' = \delta\omega_q - i\frac{\Gamma_2}{z_0}, \quad z_0 = \tanh\left(\frac{\hbar\omega_q}{2k_BT}\right), \quad \Gamma_2 = \Gamma_\phi + \frac{\Gamma_1}{2}. \tag{A7}$$

The meaning of the value z_0 lies in describing the qubit temperature-dependent equilibrium population, which is seen from Eq. (A6c), if the coupling g is neglected.

The system of equations contained in Eq. (A6) becomes closed under the assumption that all the correlation functions factorize (e.g., Ref. [36]). Then, for the classical variables

$$\alpha = \langle a\rangle, \quad s = \langle\sigma\rangle, \quad s_z = \langle\sigma_z\rangle, \tag{A8}$$

we obtain the following equations, which are also called the Maxwell-Bloch equations:

$$\dot{\alpha} = -i\delta\omega_r'\alpha - igs - i\xi, \tag{A9a}$$

$$\dot{s} = -i\delta\omega_q's + ig\alpha s_z, \tag{A9b}$$

$$\dot{s}_z = -i2g(\alpha s^* - \alpha^* s) - \Gamma_1\left(1 + \frac{s_z}{z_0}\right). \tag{A9c}$$

This system of equations is convenient for describing the dynamics, as we do in the main text. Also, these equations are simplified for the steady state, where the time derivatives on the l.h.s. are zero. Then, for α and s_z, we obtain

$$\alpha = -\xi\frac{\delta\omega_q'}{s_zg^2 + \delta\omega_q'\delta\omega_r'}, \tag{A10}$$

$$s_z = -z_0 + \frac{2z_0}{\Gamma_1}(\kappa|\alpha|^2 + 2\xi\,{\rm Im}\,\alpha). \tag{A11}$$

These are further simplified in the low-probing-amplitude limit. In this case, we note that $\alpha \sim \xi$ and obtain

$$s_z = -z_0, \tag{A12}$$

$$\alpha = \xi\frac{\delta\omega_q'}{z_0g^2 - \delta\omega_q'\delta\omega_r'}. \tag{A13}$$

These formulas are analyzed in the main text.

APPENDIX B: SEMIQUANTUM MODEL WITH TEMPERATURE

Here, following Refs. [17,37], we obtain equations in the so-called semiquantum model. This model essentially takes into account the two-operator correlations, which were ignored in the semiclassical approximation given previously.

We consider the situation when the qubit-resonator detuning $\Delta = \hbar(\omega_q - \omega_r)$ is much larger than the coupling

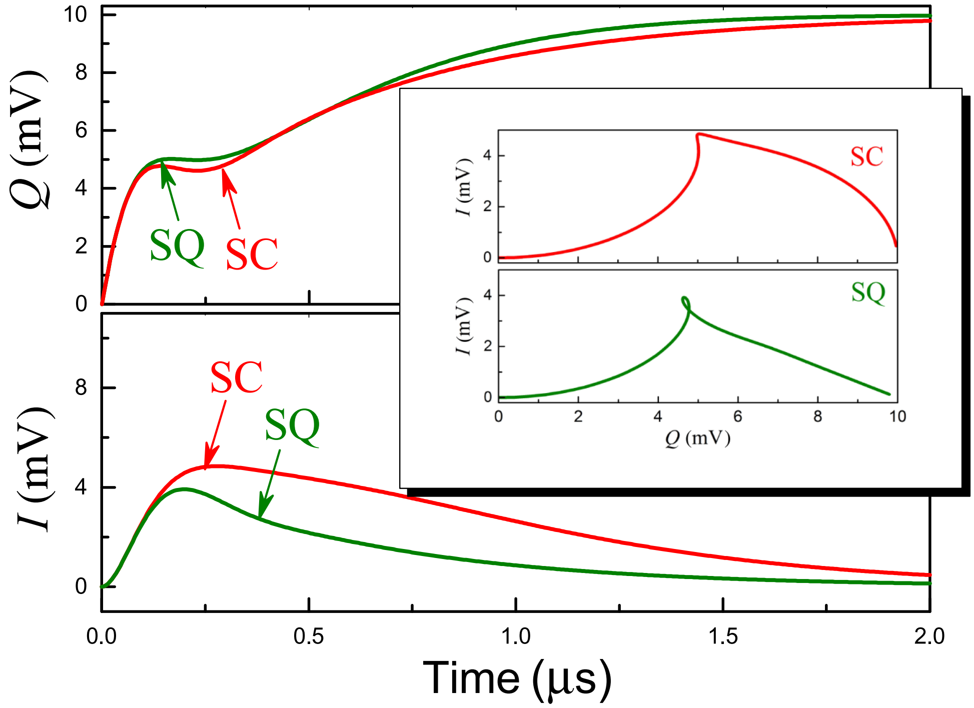

FIG. 8. Time dependence of the quadratures calculated in the semiclassical (SC) and semiquantum (SQ) approximations, where the upper panel presents the Q quadrature and lower panel presents the I quadrature. In the inset, the dynamics of the quadratures are presented in the IQ plane, where the upper panel presents the semiclassical approximation and the lower panel presents the semiquantum calculations.

strength g. The system is then described by the dispersive approximation of the Jaynes-Cummings Hamiltonian [1,17]

$$H = \hbar(\omega_r + \chi\sigma_z)a^\dagger a + \hbar\frac{\omega_q + \chi}{2}\sigma_z + \hbar\left(\xi a^\dagger e^{-i\omega t} + \frac{\Omega}{2}\sigma^\dagger e^{-i\omega_d t} + \text{H.c.}\right). \tag{B1}$$

Here, the second line represents the two control fields. The full Hamiltonian H of the system can be transformed using the operator $U = \exp[it(\omega a^\dagger a + \omega_d\sigma_z/2)]$ to the following $H' = UHU^\dagger + i\hbar\dot{U}U^\dagger$:

$$H' = \hbar(\delta\omega_r + \chi\sigma_z)a^\dagger a + \hbar\frac{\delta\omega_{q-d} + \chi}{2}\sigma_z + \hbar\xi(a^\dagger + a) + \hbar\frac{\Omega}{2}(\sigma + \sigma^\dagger), \tag{B2}$$

where $\delta\omega_{q-d} = \omega_q - \omega_d$. Following Ref. [17], now for nonzero temperature, from the Lindblad equation, Eq. (A3), for the expectation values of the operators $\langle\sigma_i\rangle$ $(i = x, y, z)$ and the resonator field operators $\langle a\sigma_i\rangle$ and $\langle a^\dagger a\rangle$, we obtain the following system of equations:

$$\frac{d}{dt}\langle\sigma_z\rangle = \Omega\langle\sigma_y\rangle - \Gamma_1\left(1 + \frac{\langle\sigma_z\rangle}{z_0}\right), \tag{B3a}$$

$$\frac{d}{dt}\langle\sigma_x\rangle = -(2\chi\langle a^\dagger a\rangle + \delta\omega_{q-d} + \chi)\langle\sigma_y\rangle - \Gamma_2\frac{\langle\sigma_x\rangle}{z_0}, \tag{B3b}$$

$$\frac{d}{dt}\langle\sigma_y\rangle = (2\chi\langle a^\dagger a\rangle + \delta\omega_{q-d} + \chi)\langle\sigma_x\rangle - \Gamma_2\frac{\langle\sigma_y\rangle}{z_0} - \Omega\langle\sigma_z\rangle, \tag{B3c}$$

$$\frac{d}{dt}\langle a\rangle = -i(\delta\omega_r\langle a\rangle + \chi\langle a\sigma_z\rangle + \xi) - \frac{\kappa}{2}\langle a\rangle, \tag{B3d}$$

$$\frac{d}{dt}\langle a^\dagger a\rangle = -2\xi\,\text{Im}\langle a\rangle + \kappa(N_{\text{th}} - \langle a^\dagger a\rangle), \tag{B3e}$$

$$\frac{d}{dt}\langle a\sigma_z\rangle = -i\left(\delta\omega_r\langle a\sigma_z\rangle + \chi\langle a\rangle + \xi\right)\langle\sigma_z\rangle + \Omega\langle a\sigma_y\rangle - \Gamma_1\langle a\rangle - \left(\frac{\Gamma_1}{z_0} + \frac{\kappa}{2}\right)\langle a\sigma_z\rangle, \tag{B3f}$$

$$\frac{d}{dt}\langle a\sigma_x\rangle = -i\delta\omega_r\langle a\sigma_x\rangle - \left(\frac{\Gamma_2}{z_0} + \frac{\kappa}{2}\right)\langle a\sigma_x\rangle + [\delta\omega_{q-d} + 2\chi(\langle a^\dagger a\rangle + 1)]\langle a\sigma_y\rangle - i\xi\langle\sigma_x\rangle, \tag{B3g}$$

$$\frac{d}{dt}\langle a\sigma_y\rangle = -i\delta\omega_r\langle a\sigma_y\rangle - \left(\frac{\Gamma_2}{z_0} + \frac{\kappa}{2}\right)\langle a\sigma_y\rangle - i\xi\langle\sigma_y\rangle - \Omega\langle a\sigma_z\rangle \tag{B3h}$$

$$-[\delta\omega_{q-d} + 2\chi(\langle a^{\dagger}a\rangle + 1)]\langle a\sigma_x\rangle. \qquad \text{(B3i)}$$

Here, we have truncated the infinite series of equations by factoring the higher-order terms $\langle a^{\dagger}a\sigma_i\rangle \approx \langle a^{\dagger}a\rangle\langle\sigma_i\rangle$ and $\langle a^{\dagger}aa\sigma_i\rangle \approx \langle a^{\dagger}a\rangle\langle a\sigma_i\rangle$. Note that at $T = 0$, the system given in Eq. (B3) coincides with Eq. (5) of Ref. [17].

We have numerically solved the system of equations given in Eq. (B3) and the results are shown in Fig. 8. The two main panels present the dynamics of the quadratures, where the red curves are the result of calculations in the semiclassical approximation, demonstrated in the main text in Fig. 1. The green curves present the dynamics of the quadratures calculated in the semiquantum approximation. There is good quantitative agreement between the two approximations for the Q quadrature, while the agreement for the I quadrature during the transient stage is only qualitative. In addition, to further emphasize the similarity of and distinction between the two approaches, we present these quadratures in the inset of Fig. 8. While the two approaches give similar dynamics for the quadratures, the semiclassical approximation does not describe the self-crossing of the IQ curve. Such a dependence, including the self-crossing feature, has been demonstrated in Fig. 4(d) of Ref. [17]. We can draw the conclusion here that the semiclassical approximation is good for obtaining analytic expressions, which describe qubit-resonator dynamics, while for describing some of the fine features of the dynamics, semiquantum calculations may be necessary. Most importantly, we can see that the semiclassical approximation gives the correct values for the stationary variables.

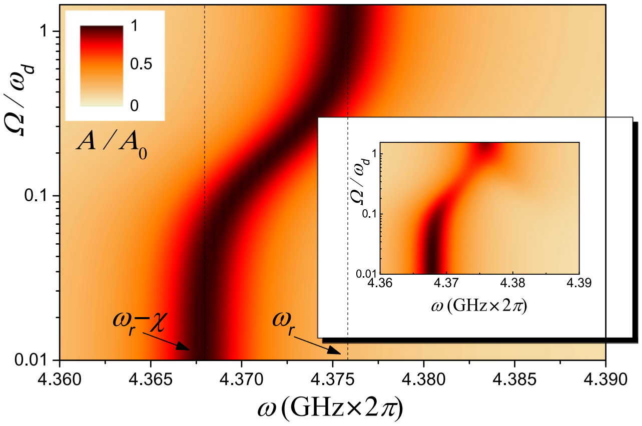

FIG. 9. The resonant-frequency shift for the strongly driven qubit-resonator system. The transmission amplitude A is plotted as a function of the probing frequency ω and the driving amplitude Ω for the off-resonant driving with $\omega_d \neq \omega_q$. Semiclassical and semiquantum calculations are presented in the main panel and in the inset, respectively.

APPENDIX C: QUANTUM-TO-CLASSICAL TRANSITION FOR THE STRONGLY DRIVEN QUBIT-RESONATOR SYSTEM

In order to further demonstrate our approach, we devote this Appendix to the regime of strong driving of the qubit-resonator system. The frequency shift of the resonant transmission through the system was recently studied in detail in Refs. [21,51]. There, the authors studied such a quantum-to-classical transition both experimentally and theoretically. Importantly, they compared several numerical approaches, with rotating-wave approximation and without, taking into account both two transmon levels only and also higher levels. Our calculations are rather analytic and comparing them with those of Refs. [21,51] shows both the applicability and the limitations of our approach.

Therefore, for our calculations we took the parameters close to those Ref. [21]: $\omega_r/2\pi = 4.376$ GHz, $\omega_q/2\pi = 5.16$ GHz, $g/2\pi = 80$ MHz (which gives $\chi/2\pi = 8.2$ MHz), $\kappa/2\pi = 4$ MHz, $\Gamma_1/2\pi = 2$ MHz, $\Gamma_2 = \Gamma_1$, and also driving frequency $\omega_d = 4.35$ GHz $\times\, 2\pi$. For this off-resonant driving ($\omega_d \neq \omega_q$), we make use of Eq. (13) and then, together with Eq. (7), we plot the transmission amplitude in the main panel in Fig. 9. This figure displays the transition from low-amplitude driving, when the resonant transmission appears around $\omega = \omega_r - \chi$, corresponding to the qubit in the ground state, to high-amplitude driving, when the qubit is in the superposition state, with average $P_+ = 1/2$, and the resonant transition appears around $\omega = \omega_r$. One can observe that with an increase of the driving amplitude Ω, the frequency shifts by the value χ, which is defined in Eq. (8), $\chi = g_0^2 E_c/\Delta(\Delta - E_c)$. We must note that for resonant driving, with $\omega_d = \omega_q$, it is much easier to saturate the qubit population, and this happens at a much smaller driving power, at $\Omega \sim 0.001\omega_d \sim 2\sqrt{\Gamma_1\Gamma_2}$, rather than at $\Omega \sim \omega_d$ in Fig. 9. Therefore it is nonresonant driving that allows consideration of the resonance shift in the regime of strong driving [47].

In addition to the semiclassical calculations, in the inset of Fig. 9 we present the resonant-frequency shift in the semiquantum approximation, for which we have solved the system of equations given in Eq. (B3). Overall, the shift of the resonance is consistent with the semiclassical calculations in the main part of Fig. 9; the suppression of the peak in the crossover region makes for a closer resemblance to the experimental results and numerical calculations in Ref. [21].

---

[1] J. Koch, T. M. Yu, J. Gambetta, A. A. Houck, D. I. Schuster, J. Majer, A. Blais, M. H. Devoret, S. M. Girvin, and R. J. Schoelkopf, Charge-insensitive qubit design derived from the Cooper pair box, Phys. Rev. A **76**, 042319 (2007).

[2] S. Ashhab and F. Nori, Qubit-oscillator systems in the ultrastrong-coupling regime and their potential for preparing nonclassical states, Phys. Rev. A **A81**, 042311 (2010).

[3] G. Wendin, Quantum information processing with superconducting circuits: A review, Rep. Prog. Phys. **80**, 106001 (2017).

[4] F. Giazotto, T. T. Heikkilä, A. Luukanen, A. M. Savin, and J. P. Pekola, Opportunities for mesoscopics in thermometry and refrigeration: Physics and applications, Rev. Mod. Phys. **78**, 217 (2006).

[5] T. Albash, V. Martin-Mayor, and I. Hen, Temperature Scaling Law for Quantum Annealing Optimizers, Phys. Rev. Lett. **119**, 110502 (2017).

[6] C. M. Wilson, G. Johansson, T. Duty, F. Persson, M. Sandberg, and P. Delsing, Dressed relaxation and dephasing in a strongly driven two-level system, Phys. Rev. B **B81**, 024520 (2010).

[7] P. Forn-Diaz, J. J. Garcia-Ripoll, B. Peropadre, J.-L. Orgiazzi, M. A. Yurtalan, R. Belyansky, C. M. Wilson, and A. Lupascu, Ultrastrong coupling of a single artificial atom to an electromagnetic continuum in the nonperturbative regime, Nat. Phys. **13**, 39 (2017).

[8] J. Stehlik, Y.-Y. Liu, C. Eichler, T. R. Hartke, X. Mi, M. J. Gullans, J. M. Taylor, and J. R. Petta, Double Quantum dot Floquet Gain Medium, Phys. Rev. X **6**, 041027 (2016).

[9] A. Palacios-Laloy, F. Mallet, F. Nguyen, F. Ong, P. Bertet, D. Vion, and D. Esteve, Spectral measurement of the thermal excitation of a superconducting qubit, Phys. Scripta **T137**, 014015 (2009).

[10] J. M. Fink, L. Steffen, P. Studer, L. S. Bishop, M. Baur, R. Bianchetti, D. Bozyigit, C. Lang, S. Filipp, P. J. Leek, and A. Wallraff, Quantum-to-Classical Transition in Cavity Quantum Electrodynamics, Phys. Rev. Lett. **105**, 163601 (2010).

[11] M. Brunelli, S. Olivares, and M. G. A. Paris, Qubit thermometry for micromechanical resonators, Phys. Rev. A **84**, 032105 (2011).

[12] K. D. B. Higgins, B. W. Lovett, and E. M. Gauger, Quantum thermometry using the ac Stark shift within the Rabi model, Phys. Rev. B **88**, 155409 (2013).

[13] S. Ashhab, Landau-Zener transitions in a two-level system coupled to a finite-temperature harmonic oscillator, Phys. Rev. A **90**, 062120 (2014).

[14] S. Jevtic, D. Newman, T. Rudolph, and T. M. Stace, Single-qubit thermometry, Phys. Rev. A **91**, 012331 (2015).

[15] I. Ahmed, A. Chatterjee, S. Barraud, J. J. L. Morton, J. A. Haigh, and M. F. Gonzalez-Zalba, Primary thermometry of a single reservoir using cyclic electron tunneling in a CMOS transistor, arXiv:1805.03443.

[16] X. Mi, J. V. Cady, D. M. Zajac, P. W. Deelman, and J. R. Petta, Strong coupling of a single electron in silicon to a microwave photon, Science **355**, 156 (2016).

[17] R. Bianchetti, S. Filipp, M. Baur, J. M. Fink, M. Göppl, P. J. Leek, L. Steffen, A. Blais, and A. Wallraff, Dynamics of dispersive single-qubit readout in circuit quantum electrodynamics, Phys. Rev. A **80**, 043840 (2009).

[18] M. Gong, Y. Zhou, D. Lan, Y. Fan, J. Pan, H. Yu, J. Chen, G. Sun, Y. Yu, S. Han, and P. Wu, Landau-Zener-Stückelberg-Majorana interference in a 3D transmon driven by a chirped microwave, Appl. Phys. Lett. **108**, 112602 (2016).

[19] S. V. Remizov, D. S. Shapiro, and A. N. Rubtsov, Role of qubit-cavity entanglement for switching dynamics of quantum interfaces in superconductor metamaterials, JETP Lett. **105**, 130 (2017).

[20] X. Y. Jin, A. Kamal, A. P. Sears, T. Gudmundsen, D. Hover, J. Miloshi, R. Slattery, F. Yan, J. Yoder, T. P. Orlando, S. Gustavsson, and W. D. Oliver, Thermal and Residual Excited-State Population in a 3D Transmon Qubit, Phys. Rev. Lett. **114**, 240501 (2015).

[21] I. Pietikäinen, S. Danilin, K. S. Kumar, A. Vepsäläinen, D. S. Golubev, J. Tuorila, and G. S. Paraoanu, Observation of the Bloch-Siegert shift in a driven quantum-to-classical transition, Phys. Rev. B **96**, 020501 (2017).

[22] M. Di Ventra, Y. V. Pershin, and L. O. Chua, Circuit elements with memory: Memristors, memcapacitors, and meminductors, Proc. IEEE **97**, 1717 (2009).

[23] Y. V. Pershin and M. Di Ventra, Memory effects in complex materials and nanoscale systems, Adv. Phys. **60**, 145 (2011).

[24] S. Peotta and M. Di Ventra, Superconducting Memristors, Phys. Rev. Appl. **2**, 034011 (2014).

[25] C. Guarcello, P. Solinas, M. Di Ventra, and F. Giazotto, Solitonic Josephson-based meminductive systems, Sci. Rep. **7**, 46736 (2017).

[26] C. Guarcello, P. Solinas, M. Di Ventra, and F. Giazotto, Hysteretic Superconducting Heat-Flux Quantum Modulator, Phys. Rev. Appl. **7**, 044021 (2017).

[27] P. Pfeiffer, I. L. Egusquiza, M. Di Ventra, M. Sanz, and E. Solano, Quantum memristors, Sci. Rep. **6**, 29507 (2016).

[28] S. N. Shevchenko, Y. V. Pershin, and F. Nori, Qubit-Based Memcapacitors and Meminductors, Phys. Rev. Appl. **6**, 014006 (2016).

[29] J. Salmilehto, F. Deppe, M. Di Ventra, M. Sanz, and E. Solano, Quantum memristors with superconducting circuits, Sci. Rep. **7**, 42044 (2017).

[30] Y. Li, G. W. Holloway, S. C. Benjamin, G. A. D. Briggs, J. Baugh, and J. A. Mol, Double quantum dot memristor, Phys. Rev. B **96**, 075446 (2017).

[31] M. Sanz, L. Lamata, and E. Solano, Quantum memristors in quantum photonics, APL Photon. 3, 080801 (2018).

[32] L. S. Bishop, J. M. Chow, J. Koch, A. A. Houck, M. H. Devoret, E. Thuneberg, S. M. Girvin, and R. J. Schoelkopf, Nonlinear response of the vacuum Rabi resonance, Nat. Phys. **5**, 105 (2009).

[33] W. P. Schleich, *Quantum Optics in Phase Space* (Wiley-VCH, Berlin, 2001).

[34] S. N. Shevchenko, G. Oelsner, Y. S. Greenberg, P. Macha, D. S. Karpov, M. Grajcar, U. Hübner, A. N. Omelyanchouk, and E. Il'ichev, Amplification and attenuation of a probe signal by doubly dressed states, Phys. Rev. B **89**, 184504 (2014).

[35] Y. Mu and C. M. Savage, One-atom lasers, Phys. Rev. A **46**, 5944 (1992).

[36] J. Hauss, A. Fedorov, S. André, V. Brosco, C. Hutter, R. Kothari, S. Yeshwanth, A. Shnirman, and G. Schön, Dissipation in circuit quantum electrodynamics: Lasing and cooling of a low-frequency oscillator, New J. Phys. **10**, 095018 (2008).

[37] S. André, V. Brosco, M. Marthaler, A. Shnirman, and G. Schön, Few-qubit lasing in circuit QED, Phys. Scripta **T137**, 014016 (2009).

[38] P. Macha, G. Oelsner, J.-M. Reiner, M. Marthaler, S. André, G. Schön, U. Hübner, H.-G. Meyer, E. Il'ichev, and A. V. Ustinov, Implementation of a quantum metamaterial using superconducting qubits, Nat. Commun. **5**, 5146 (2014).

[39] R. A. Bianchetti, Ph.D. thesis, ETH Zurich, 2010.

[40] M. D. Reed, L. DiCarlo, B. R. Johnson, L. Sun, D. I. Schuster, L. Frunzio, and R. J. Schoelkopf, High-Fidelity Readout in Circuit Quantum Electrodynamics Using the Jaynes-Cummings Nonlinearity, Phys. Rev. Lett. **105**, 173601 (2010).

[41] M. Jerger, P. Macha, A. R. Hamann, Y. Reshitnyk, K. Juliusson, and A. Fedorov, Realization of a Binary-Outcome Projection Measurement of a Three-Level Superconducting Quantum System, Phys. Rev. Appl. **6**, 014014 (2016).

[42] M. Jerger, Y. Reshitnyk, M. Oppliger, A. Potocnik, M. Mondal, A. Wallraff, K. Goodenough, S. Wehner, K. Juliusson, N. K. Langford, and A. Fedorov, Contextuality without nonlocality in a superconducting quantum system, Nat. Commun. **7**, 12930 (2016).

[43] M. Reagor, W. Pfaff, C. Axline, R. W. Heeres, N. Ofek, K. Sliwa, E. Holland, C. Wang, J. Blumoff, K. Chou, M. J. Hatridge, L. Frunzio, M. H. Devoret, L. Jiang, and R. J. Schoelkopf, Quantum memory with millisecond coherence in circuit QED, Phys. Rev. B **B94**, 014506 (2016).

[44] R. Vijay, D. H. Slichter, and I. Siddiqi, Observation of Quantum Jumps in a Superconducting Artificial Atom, Phys. Rev. Lett. **106**, 110502 (2011).

[45] S. Filipp, P. Maurer, P. J. Leek, M. Baur, R. Bianchetti, J. M. Fink, M. Göppl, L. Steffen, J. M. Gambetta, A. Blais, and A. Wallraff, Two-Qubit State Tomography Using a Joint Dispersive Readout, Phys. Rev. Lett. **102**, 200402 (2009).

[46] D. T. McClure, H. Paik, L. S. Bishop, M. Steffen, J. M. Chow, and J. M. Gambetta, Rapid Driven Reset of a Qubit Readout Resonator, Phys. Rev. Appl. **5**, 011001 (2016).

[47] M. Jerger, Z. Vasselin, and A. Fedorov, *In situ* characterization of qubit control lines: A qubit as a vector network analyzer, arXiv:1706.05829.

[48] X. J. Lu, M. Li, Z. Y. Zhao, C. L. Zhang, H. P. Han, Z. B. Feng, and Y. Q. Zhou, Nonleaky and accelerated population transfer in a transmon qutrit, Phys. Rev. A **96**, 023843 (2017).

[49] K. Dai, H. Wu, P. Zhao, M. Li, Q. Liu, G. Xue, X. Tan, H. Yu, and Y. Yu, Quantum simulation of general semi-classical Rabi model beyond strong driving regime, Appl. Phys. Lett. **111**, 242601 (2017).

[50] M. J. Peterer, S. J. Bader, X. Jin, F. Yan, A. Kamal, T. J. Gudmundsen, P. J. Leek, T. P. Orlando, W. D. Oliver, and S. Gustavsson, Coherence and Decay of Higher Energy Levels of a Superconducting Transmon Qubit, Phys. Rev. Lett. **114**, 010501 (2015).

[51] I. Pietikäinen, S. Danilin, K. S. Kumar, J. Tuorila, and G. S. Paraoanu, Multilevel effects in a driven generalized Rabi model, J. Low. Temp. Phys. **191**, 354 (2018).

[52] M. O. Scully and M. S. Zubairy, *Quantum Optics* (Cambridge University Press, Cambridge, 1997).